Treatment of saline produced water through photocatalysis using rGO-TiO_2 nanocomposites

Mario Andreozzi[a], Mayra G. Álvarez[b2], Sandra Contreras[b], Francesc Medina[b], Laura Clarizia[a], Giuseppe Vitiello[a,c], Jordi Llorca[d], Raffaele Marotta[a,1]

[a] Department of Chemical Engineering, Materials and Industrial Production (DICMAPI), University of Naples Federico II, p.le V. Tecchio 80 - 80125 Napoli, Italy.

[b] Departament d'Enginyeria Química, Universitat Rovira i Virgili, Campus Sescelades. Avda, Països Catalans, 26, Tarragona, Spain.

[c] Consorzio Interuniversitario per lo Sviluppo dei Sistemi a Grande Interfase (CSGI), via della Lastruccia 3, 50019 Sesto Fiorentino, Florence, Italy.

[d] Institute of Energy Technologies, Department of Chemical Engineering and Barcelona Research Center in Multiscale Science and Engineering, Universitat Politècnica de Catalunya, EEBE, Eduard Maristany 10-14, 08019 Barcelona, Spain

[1] *first corresponding author* (Marotta R.): raffaele.marotta@unina.it

[2] *second corresponding author* (Alvarez M.G.): mayra.garcia@urv.cat

ABSTRACT

Graphene like-TiO_2 nanocomposites (rGO-TiO_2) are prepared via hydrothermal route by following different synthetic protocols. The as-prepared nanostructured materials exhibit higher photocatalytic activity than bare TiO_2 in the treatment of synthetic produced water containing high salinity levels and different compositions of recalcitrant dissolved organic matter. The effect of the preparation method on the physico-chemical properties is assessed by performing a wide characterization

combining different analyses, such as nitrogen physic-adsorption (BET), X-ray Diffraction (XRD), Transmission Electron Microscopy (TEM), UV-VIS Diffuse Reflectance Spectroscopy (DRUV) and Electron Paramagnetic Resonance (EPR). The effect of several operative variables (i.e., TiO_2/rGO weight ratios, and addition of hydrogen peroxide) on the photocatalytic activity is also critically evaluated.

The highest photocatalytic activity is obtained for a rGO/TiO_2 weight ratio of about 10%, for which a good compromise between uniformity of dispersion of the TiO_2 particles on the rGO layers and covering degree of the titania photoactive surface is achieved.

This study can contribute to open new perspectives in the design of high performance graphene like-based TiO_2 photocatalysts for removing hydrophobic bio-recalcitrant pollutants from saline water.

Keyword: saline produced water, photocatalysis, TiO_2/rGO, graphenic materials, hydrophobic organic pollutants, water reuse.

1. Introduction

Heterogeneous TiO_2-based photocatalysis is one of the most used photocatalytic processes for wastewater treatment and water reuse due to the relative great abundance, high chemical stability, cheapness and low environmental impact of titanium dioxide [1]. In particular, this technology has demonstrated to have high potential for removing persistent organic pollutants (POPs) and compounds highly resistant to conventional biological treatments [2].

However, some major drawbacks limit the use of titanium dioxide in commercial applications [3]. Firstly, due to its wide band gap (3.2 eV), titanium dioxide requires light irradiation with wavelengths shorter than 387 nm (UVA) for its photoactivation. As the UVA component accounts for only about 5% of the total solar spectrum at sea level, severe limitations for solar implementations remain. Moreover, poor adsorption capacity for hydrophobic contaminants and

low photonic efficiencies due to prompt recombination of photogenerated electron/hole pairs are recorded during water treatment processes over TiO_2 photocatalysts. In order to reduce such limitations and consequently increase the photocatalytic efficiency of titanium dioxide, several investigations have been recently carried out [4,5]. It has been demonstrated that the addition of graphitic materials to titanium dioxide is one of the most valuable methods to improve the photocatalytic efficiency of pristine TiO_2, due to the increased specific surface area and mobility of charge carriers [6,7]. In particular, graphene and reduced graphene oxide have been recently used as supports for loading titania particles due to their superior conductive, mechanical, and chemical properties [8-14].

Among industrial aqueous effluents containing persistent and biorefractory organic pollutants, saline produced water (SPW) has the largest annual volumetric flow (77 billion of liter per year [15]) and therefore poses serious environmental and operational problems [16].

Saline produced water is normally generated when saline water and hydrocarbons are mixed during the extraction of natural gas and crude oil.

Saline produced water usually contains organic species (aromatic hydrocarbons, phenols, organic acids, etc), inorganic compounds (metals, salts), and solid particles due to leaching of rocks [17].

The ecotoxicological effects of produced water and the growing depletion of water resources, especially for oil producing countries with water scarcity make it necessary to treat produced water.

Physico-chemical and biological processes are conventionally employed for treating SPW [18]. However, physico-chemical technologies are preferred in offshore facilities due to space requirements. Electrochemical, Fenton, and ozonation processes, based on the chemical oxidation of the organic contaminants dissolved in SPWs, are the most investigated chemical techniques [19]. However, the high cost of chemicals and the formation of considerable amounts of sludge limit the application of these methods. Few research efforts have been carried out for treating produced water by photocatalytic processes [20-22]. The studies demonstrated that these processes can be applied to the treatment of saline produced water. Nevertheless, the use of photocatalysis with pristine TiO_2 is

often characterized by low efficiency and poor decrease in toxicity of the treated effluents due to (*i*) the high rate of photogenerated electron/hole recombination, (*ii*) the poor capacity of adsorption of the pollutants, and (*iii*) the high concentration of chloride ions in SPW which act as $HO^{\cdot}$ radical scavengers and compete with organic substrates [23].

The present paper aims at investigating (*i*) the photocatalytic treatment of synthetic SPW using two different titanium dioxide photocatalysts doped with reduced graphene oxide (rGO) and (*ii*) the effect of some experimental variables, such as different nature of titania (commercial P25 or home prepared anatase TiO_2), rGO/TiO_2 weight ratio, and the addition of H_2O_2, in the photocatalytic treatment of SPW.

2. Materials and methods

2.1. Materials

Sea-water samples were collected in the Mediterranean Sea (800 meters from Barcelona coast and 30 meters deep). A chemical characterization of the sea-water is reported in Table S1.

Acetic acid (AcH ≥99.5%), phenol (≥99.0%), toluene (99.8%), naphthalene (99%), (o, m, p)-xylene (99%), TiO_2 Aeroxide-P25 (80/20 anatase/rutile), formamide (≥99.5), 2-Propanol (IPA, ≥ 99.5%), titanium isopropoxide (TTiP, ≥ 97%), triethylamine (TEA, ≥ 99.5%), ethanol (96%) and Triton X were purchased from Sigma-Aldrich and used without further purification. Natural graphite (carbon content: 99.8%, 325 mesh) was purchased from Alfa-Aesar. MilliQ water (Q-Gard 1 Purification Cartridge) was used for the preparation of the reacting mixtures for comparative purposes.

2.2. Catalyst preparation

Reduced graphene oxide/commercial titania (rGO/TiO_2-P25): The catalyst was prepared starting from graphene oxide (GO) and P25 by hydrothermal treatment. GO was synthesized from graphite using a modified Hummers method [24]. Details of the synthesis can be found in previous papers [25,45]. A proper amount of GO was dispersed in 50 mL of MilliQ water and 20 mL of formamide

for 1 h with magnetical stirring at room temperature. The mixture was ultrasonicated (Ultrasonic processor, 180 W, frequency 24 kHz) for 1 h, after which TiO_2-P25 (1 g) was added. After stirring (2 h) and successive ultrasonication (1 h), the suspension was introduced in a Teflon lined autoclave reactor and hydrothermally treated at 120 °C for 18 h. The solid obtained was firstly filtered with porous glass funnel under reduced pressure and washed with 1L of MilliQ water, right after with 200 mL of ethanol and finally dried at 60 °C for 18 h.

2.3. Reduced graphene oxide/home made titania (rGO/TiO_2-HM):

TiO_2-HM and rGO/TiO_2-HM catalysts were prepared by hydrothermal synthesis [26-27]. Firstly, TiO_2-HM was prepared as in the references. A typical precursor solution was obtained by adding dropwise 6 mL of TTiP/IPA solution (Sol-1, 3.38 M in TTiP) to 31.3 mL of water solution at pH 1.5 achieved by means of AcH (Sol-2). After Sol-1 addition a white precipitate was obtained. After stirring at room temperature for two days, the formation of a yellowish colloidal solution indicated resuspension of the precipitate and reduction in particles size below 20 nm [28]. TEA was then added dropwise to the TiO_2 colloidal solution until pH=7. The obtained white precipitate suspension was then sealed within a Teflon recipient (the liquid volume corresponding to 75% of the whole), placed into a circulating oven, and kept at 120 °C for 24 h. TiO_2 powders were obtained by centrifugation and repeated washing (3 times with distilled water). The obtained precipitates were dried at 90 °C.

Reduced graphene oxide/home made titania (rGO/TiO_2-HM) catalyst was prepared *in situ* by following almost the same procedure as bare TiO_2. Briefly, Sol-1 (6 mL) was added drop-wise to Sol-2 (31.3 mL) and the mixture was kept stirred for two days leading to TiO_2 colloidal solution. Then, an appropriate amount of graphene oxide (GO) for 1.193 mL of TTiP was added in order to obtain the final systems with different percentage content of rGO, varying from 1 to 20 w/w %. Then, 20 mL of formamide were added to the mixture just before neutralization with TEA until pH

7. Finally, the obtained suspension was sealed within a Teflon recipient (the liquid phase consisting of 75% of the whole volume), placed into a circulating oven and kept at 120 °C for 24 h [27].

2.4. Preparation of SPW

SPW was prepared according to the bibliographic data of oilfields PW [19,29,48–51], considering the main groups of dissolved organic components usually present in PW (BTEX, PAHs, organic acids and phenols) and their concentrations; hence the O&G group was excluded here, as this fraction would have been removed in a previous pretreatment unit. In particular, synthetic contaminated solutions were prepared in a 1000 mL volumetric flask starting either from sea-water samples from the Mediterranean sea (SPW) or from MilliQ water and adding the different organic substrates to obtain a final aqueous solution of acetic acid (150 mg/L), phenol (10 mg/L), toluene (10 mg/L), (o, m, p)-xylenes (10 mg/L) and naphthalene (3 mg/L). Due to the very low solubility of naphthalene in water, a mother solution containing 31 ppm of naphthalene (in seawater or MilliQ depending on the test) with 10 μL/L of surfactant Triton X was previously prepared. The solution was mixed with a homogenizer (Homogenizer 850 Fischer Scientific) at 6000 rpm for 15 min.

2.5. Analytical procedures

Structural and compositional characterization of the photocatalysts was performed by X-ray diffraction (XRD), Brunauer–Emmett–Teller (BET) N_2 adsorption analysis, scanning electron microscopy (SEM) and transmission electron microscopy (TEM).

XRD measurements were carried out by a Bruker-AXS D8-Discover diffractometer with a vertical theta–theta goniometer and a Vantec linear detector. Monochromatic Cu Kα radiation was obtained from a copper X-ray tube operated at 40 kV and 40 mA and a Nimonochromator. Data were recorded over a 2θ range of 5–70° with an angular step of 0.02° at 10.6 s/step.

Crystallite size and crystalline phase contents were calculated by means of the program TOPAS working under the programming mode (launch mode) with local routines. The crystallite sizes estimated for all phases were calculated using the integral breadth method so that the crystallite size

is the average taking into account all the diffraction peaks. Using integral breadth instead of FWHM may reduce the effect of crystallite size distribution on the Scherrer constant K and therefore the crystallite size analysis is more accurate. Specific surface areas were determined by nitrogen adsorption at −196 °C using a Micromeritics ASAP 2020 automatic analyzer. Samples were previously degassed in situ at 150 °C under vacuum for 15 h. Surface areas were calculated using the Brunauer–Emmet–Teller (BET) method over a p/p° range where a linear relationship was maintained. Morphology of the samples was analyzed by electron microscopy. Transmission electron microscopy (TEM) was performed in the bright field by using a JEOL JEM-2100 instrument at an accelerating voltage of 100 kV. The samples were prepared by dispersing the as-prepared catalysts in ethanol and then drop casting the suspension on a standard 3 mm holey copper grid and letting the ethanol evaporate at room temperature.

HRTEM and SAED patterns were performed with a FEI Tecnai F20 microscope equipped with a field emission electron gun and operating at 200 kV. For that, selected samples were dispersed in an alcohol suspension and a drop of the suspension was placed over a grid with holey-carbon film.

EDX was performed on the samples in ESEM using a FEI Quanta 600 microscope equipped with energy dispersive X-ray microanalysis from Oxford Instruments operating at high vacuum with an accelerating voltage of 20 kV and a working distance of 6.6 mm.

Diffuse Reflectance UV–Vis (DRUV) measurements were performed to establish the optical band gap by using a Jasco spectrophotometer and $BaSO_4$ as a reference. The optical absorption was measured in the 190–850 nm wavelengths range.

Electron Paramagnetic Resonance (EPR) spectroscopy experiments were carried out by means of X-band (9 GHz) Bruker Elexys E-500 spectrometer (Bruker, Rheinstetten, Germany), equipped with a super-high sensitivity probe head. Solid samples were transferred to flame-sealed glass capillaries which, in turn, were coaxially inserted in a standard 4 mm quartz sample tube. Measurements were performed at room temperature. The instrumental settings were as follows:

sweep width, 1500 G; resolution, 1024 points; modulation frequency, 100 kHz; modulation amplitude, 1.0 G. 16 scans were accumulated to improve the signal-to-noise ratio.

Total organic carbon (TOC) was monitored by a TOC analyzer (Shimadzu TOC- LCSN). Analysis of organic acid and phenol was performed with a HPLC system (LC Shimadzu 2010) equipped with a diode array detector (DAD) and a Mediterranea HPLC column (C18, 2.1 × 150 mm, 3.5 μm, Teknokroma, USA) thermostated at 40°C. An isocratic program for the elution was used with a flow rate of 0.8 mL/min (mobile phase: MilliQ water at pH 2.2). The DAD wavelength was set at 220 nm. BTEX and naphthalene were analyzed by gas chromatography coupled to a mass spectrometer detector (GC-MS 2010 Shimadzu) equipped with a Zebron ZB-5 column and using a splitless injection mode of 0.5 μL of sample.

2.6. Photocatalytic apparatus

Photocatalytic runs were carried out in a borosilicate (Schott Duran), magnetically stirred reactor (V, 0.6 L), thermostated at 30 °C. The reacting mixture (0.5 L) was irradiated with four low-pressure mercury-vapor fluorescent lamps (TL-D 15W BLB 1SL/25, 15.9 W), mainly emitting in the wavelength range of 350-400 nm (manufacturer's data). The total average photon flux (I_o, $2.17 \cdot 10^{-6}$ E/s, ~0.714 J/s) of the UVA-lamps was measured through actinometry by using a modified ferrioxalate procedure [30]. The method is based on the photochemical reduction of the ferrioxalate complex $[Fe(C_2O_4)_3]^{3-}$ to Fe (II) in acidic medium. The reduction takes place with a quantum yield of 1-1.2 mol/E in a wavelengths range of 250-450 nm [31]. The concentration of Fe(II) was monitored by UV-VIS spectroscopy with the o-phenanthroline method [32], based on the formation of a colored complex between Fe(II) in solution and 1,10-phenanthroline in acidic medium acetic acid/acetate at pH 3-4. A proper amount prepared photocatalyst was suspended in a synthetic SPW (0.5 L). The pH of the mixture was not regulated.

Samples were collected at selected reaction times and submitted to TOC and GC analyses. The experimental runs were carried out in duplicate and the percentage standard deviation of the

reproduced data was less than 4.6%. The efficiency was calculated at 5 hours of treatment as reported in equation 1 [33]:

$$Efficiency = \frac{TOC_{in}(ppm) - TOC_{5hrs}(ppm)}{Q_j(kWh/L)} \cdot \frac{1}{V(L)} \quad \text{eq. 1}$$

where V is the volume of the solution and Q_j is the accumulated energy, calculated as the incident average photon flux (I_o, J/s) multiplied by the treatment time (Δt, s) and divided by the volume of the solution (V, L), as reported in equation 2:

$$Q_j = \frac{I_o}{V} \cdot \Delta t \quad \text{eq. 2}$$

3. Results and discussion

3.1. Catalyst characterization

The BET surface area (*SSA*) and the total pore volume (*TPV*) of the different photocatalyst particles are reported in Table 1.

The BET surface areas of TiO_2-HM and rGO/TiO_2-HM samples are significantly larger than TiO_2-P25 and rGO/TiO_2-P25 in the whole range of RGO contents. Besides, as the rGO/TiO_2-P25 weight ratio increases from 0% to 20% in the composite, the specific surface area increases, whereas the total pore volume remains quite unchanged for values of rGO/TiO_2-P25 weight ratio higher than 5%. On the other hand, the specific surface area for rGO/TiO_2-HM samples increases with the addition of rGO with respect to bare titania and reaches the highest value for a weight ratio equal to 5%. TPV is not affected by the presence or the percentage of rGO in TiO_2-HM.

Figure 1 shows the pore size distribution curves of bare TiO_2 and rGO/TiO_2 composites. If compared with pristine TiO_2-P25, the presence of rGO in rGO/TiO_2-P25 samples determines an increase in micropores and mesopores size with mean pore sizes close to 3 nm and 18 nm, respectively (Fig. 1a). On the contrary, TiO_2-HM and rGO/TiO_2-HM samples present a rather unimodal pore size distribution (Fig. 1b) - contrary to what observed for the rGO/TiO_2-P25 materials - with mean pore diameters ranging from ca. 6 to 9 nm for rGO/TiO_2-HM composites and

bare TiO_2-HM, respectively. For TiO_2-HM based materials, the addition of reduced graphene oxide does not seem to lead to appreciable increases in volume of mesopores in accordance with the TPV values listed in Table 1.

The relatively higher presence of mesopores for rGO/TiO_2-P25 nanocomposites indicates a different morphology with respect to rGO/TiO_2-HM and, as reported by others [34], can be ascribed to interstitial zones between TiO_2-P25 particles and rGO nanosheets.

TEM and SEM images obtained for rGO/TiO_2-P25 samples are shown in Figures 2a-d and Figure 3a, respectively.

Lamellar structures of rGO are well evidenced in Figures 2b-d. For rGO/TiO_2-P25 weight ratio of 1% (Fig. 2a), only small pieces of rGO nanosheets are present among titania particles. In the sample with a rGO/TiO_2-P25 weight ratio of 5% (Fig. 2b), titania particles are almost dispersed on the surface of rGO nanosheets. This condition is better realized in the rGO/TiO_2-P25 sample with a weight ratio of 10% (Fig. 2c), where the nanolayers act as bridges between neighboring TiO_2-P25 nanoparticles. A different structure is observed in the composite with rGO/TiO_2-P25 weight ratio of 20%, where TiO_2 nanoparticles are closely wrapped in rGO nano- (Fig. 2d) and micro- (Fig. 3a) sheets.

Figures 3b and Figures 4a-f show SEM and TEM images of rGO/TiO_2-HM composites, respectively. rGO/TiO_2-HM samples contain TiO_2 nanoparticles non-uniformly dispersed on the rGO layers in all the weight ratios studied (Fig. 4a-c). The TiO_2-HM nanoparticles have nanorod shape with length less than 30 nm and non-uniform diameters (Fig. 4d). As shown in Figure 4e, TiO_2-HM nanoparticles occasionally generate chain-shaped aggregates anchored on the rGO surface. However, in general, TEM analysis suggests that *in situ* preparation of rGO/TiO_2-HM samples with rGO/TiO_2 weight ratio of 1-10% leads to structures where the dispersion of TiO_2 nanoparticles on the RGO surface is not significantly affected by rGO content. For higher rGO/TiO_2 weight ratio (20%), several disordered agglomerates of titania nanorods along wrinkles and edges of

rGO layers are noted (Figs. 4f, 3b), where a higher density of residual carboxylic groups of graphene oxide is more likely [35].

Selected samples, namely rGO(10%)/TiO_2-P25 and rGO(10%)/TiO_2-HM, were also analyzed by HRTEM. Figure 5a shows a general view of the sample prepared with commercial TiO_2 (i.e., rGO(10%)/TiO_2-P25) and the corresponding selected-area electron diffraction (SAED) pattern. The sample is comprised by a mixture of rGO and TiO_2 crystallites in the range 10-30 nm. The TiO_2 particles are perfectly crystalline and no amorphous phase is observed. The SAED pattern exhibits diffraction rings corresponding to a mixture of anatase and rutile phases, as expected from TiO_2-P25, and a diffuse ring corresponding to rGO. HRTEM images at high magnification are shown in Figures 5b-d, where a close contact between rGO and TiO_2 crystallites is observed (Figure 5b); however, some domains are also observed in this sample where both phases occur clearly separately (Figure 5c). A careful analysis of the lattice fringes reveals crystallographic planes of anatase (at 3.5 and 2.4 Å corresponding to planes (101) and (103), respectively) and rutile (at 2.5 Å corresponding to crystallographic plane (101)) phases.

Figure 6a shows a low-magnification image of the sample rGO(10%)/TiO_2-HM where an individual reduced graphene oxide sheet is covered by TiO_2 particles. The SAED pattern shows spots at 2.03 Å corresponding to the (101) crystallographic planes of rGO, indicating that the rGO sheet is oriented along the [001] crystallographic direction. In addition to the rGO spots, the SAED pattern also shows the diffraction rings of TiO_2 corresponding to anatase form. A close inspection of the sample is shown in Figure 6b, where anatase crystallites are perfectly dispersed over rGO. Contrarily to that found by conventional TEM analysis, here the TiO_2 crystallites show either a round-shaped morphology of about 5-10 nm in diameter or an elongated morphology measuring about 5 x 15 nm, approximately. From the lattice fringe analysis it is concluded that all TiO_2 particles are perfectly crystalline with no amorphous phase present. The lattice fringes at 3.5 and 2.4 Å correspond to the crystallographic planes (101) and (103) of anatase, respectively. Besides, it

should be highlighted that all the TiO_2 crystallites in this sample are in tight contact with rGO (Figures 6c-d).

XRD analysis of GO and rGO, obtained under the same preparation conditions of rGO/TiO_2 composites, demonstrate the reduction of GO during hydrothermal treatment produced by the loss of its oxidation debris. The so-obtained rather amorphous material has a broad diffraction band with low intensity in the 2ϑ angle range of 15°–30º (Fig. 7).

XRD patterns of pure TiO_2 and rGO(20%)/TiO_2 composites are shown in Figure 8. No diffraction peaks for carbon species are observed for the composites if compared with the bare TiO_2 pattern. This can be ascribed, as reported by others [36, 37], to relatively low diffraction intensities of the rGO (Fig. 7), the overlap of the rGO peak (24.5°), and the intense anatase peak at 25.4° (Fig. 8). At the same time, the rGO(20%)/TiO_2-HM composite reveals peaks that can be ascribed to titania in anatase form, whereas a mixture of anatase (86%) and rutile (14%) phases is obviously observed in the case of rGO/TiO_2-P25 sample. As expected, intensities of TiO_2 structure decreases with the increasing content of rGO in the composite. Further, the width of the anatase peaks for rGO/TiO_2-HM nanocomposites is higher than that of both TiO_2-HM and rGO/TiO_2-P25 samples, which are sharper. Two effects are responsible of the peak width produced in rGO/TiO_2-HM. On the one hand, samples prepared with TiO_2-HM present an anisotropic widening. This is notable in (*hkl*) planes which are wider, whereas (004) plane is sharper due to the elongated shape presented by TiO_2 nanoparticles in the *c* direction, as confirmed by TEM analysis. On the other hand, the average crystallite size for titania nanoparticles in rGO/TiO_2-HM composites is about 6 nm, lower than rGO/TiO_2-P25 samples (ca. 20 nm), in agreement with that observed by HRTEM.

Besides, the crystallite size also decreases from bare TiO_2-HM (ca. 9 nm) to rGO/TiO_2-HM composites (ca. 6 nm), which would explain the increased peak widths in the composite materials respect to the former.

However, the width of the peaks for rGO/TiO_2-HM nanocomposites is not influenced by the rGO/TiO_2 weight ratio, as shown in Figure 9.

EPR spectra for pure GO, as a reference, and for both rGO(10%)/TiO_2-P25 and rGO(10%)/TiO_2-HM nanocomposites are shown in Figure 10. A single peak signal is observed for pure graphene oxide, characterized by a ΔB value of 2.0±0.1 G and a *g*-factor value of 2.0035±0.0003, which is typical of carbon-centered radicals. It is in agreement with the literature [38,39] and corresponds to samples with high carbon content, which have more paramagnetic centers. A very slight signal is observed for rGO(10%)/TiO_2-P25 sample, characterized by a *g*-factor value of 2.0030±0.0003 and corresponding to oxygen vacancies in the TiO_2 [40-42]. In contrast, any signal is detectable for the rGO(10%)/TiO_2-HM system. However, any signal of carbon-centered radical is observed in the EPR spectra of both samples, clearly indicating a very low degree of defects [43] in the rGO structure within the final nanocomposites.

Diffuse Reflectance UV (DRUV) absorption spectra and plots of $(F(R)hv)^{1/2}$ versus photon energy (h*v*) for rGO(10%)/TiO_2-P25 and rGO(10%)/TiO_2-HM nanocomposites are shown in Figures 11a-b. DRUV spectra of bare TiO_2-P25 and TiO_2–HM are also shown as references. Figure 11a indicates that both rGO(10%)TiO_2-P25 and rGO(10%)TiO_2-HM samples have similar absorption spectra and only slightly absorb at higher wavelengths (λ > 400 nm) with respect to bare TiO_2-P25 and TiO_2-HM. As shown in Figure 11b, no changes in the TiO_2-P25 band gap value (~3.0 eV) are observed in the presence of rGO, whereas a slight decrease of the apparent E_g value is registered in sample rGO/TiO_2-HM compared to TiO_2–HM. This can be due to the generation of intraband gaps upon the addition of rGO in the composite or an apparent band gap produced by the superposition of absorption spectra of the different materials composing the sample rGO/TiO_2-HM.

4. Photocatalytic tests

4.1. rGO/TiO_2 nanocomposites vs bare TiO_2

Figure 12 shows the mineralization degree of the synthetic organic mixture (section 2.4) over bare TiO_2-P25 photocatalyst in MilliQ water without and with sodium chloride (35 g/L) and in sea-water (SPW) against the treatment time and the accumulated energy (*Qj*, kJ/L).

It can be observed that chloride ions have a remarkable detrimental effect on the kinetic of TOC reduction as they compete with organics to react with hydroxyl radicals (r_1) and photogenerated positive holes (r_2):

$$Cl^- + HO^\cdot \rightarrow Cl^\cdot + HO^- \quad r_1$$

$$Cl^- + h^+ \rightarrow Cl^\cdot \quad r_2$$

Furthermore, chloride ions and organic species compete for adsorbing on the photocatalyst surface. Such inhibition is even more marked in sea-water, probably due to the simultaneous presence of different inorganic anions (chloride, sulfate, carbonate, etc.). A similar effect is recorded by using bare TiO_2-HM photocatalyst (data not shown).

As shown in Figure 13, bare TiO_2-HM shows a higher activity in TOC removal if compared to bare TiO_2-P25 due to the three times larger specific surface area. However, the efficiency of TOC removal in SPW is increased in presence of rGO(10%)/TiO_2 photocatalysts, although the composite nanomaterials show higher photoactivity with trends different from the respective bare TiO_2 photocatalysts. The best result is obtained over rGO(10%)/TiO_2-P25 with a TOC removal degree higher than 20% (efficiency: $5.093 \cdot 10^3$ ppmTOC/kWh), compared to 12% of TOC removal (efficiency: $3.037 \cdot 10^3$ ppmTOC/kWh) over bare TiO_2-P25 after 5 hours of treatment. The modest increase in activity of rGO(10%)/TiO_2-HM with respect to bare TiO_2-HM confirms the synergistic effect produced by hybridization of both materials. However, the superior activity found for the catalyst prepared from P25 (rGO(10%)/TiO_2-P25) suggests that the interaction between rGO and the surface of TiO_2 is not the only parameter affecting the efficiency of the photocatalyst. Interestingly, this catalyst showed a slight EPR signal, clearly associable to the presence of oxygen vacancies [42] which were not detected for the the catalyst prepared with TiO_2-HM (rGO(10%)/TiO_2-HM); thus, the presence of such ~~a~~ EPR signal seems to be dependent but not solely related to the presence of rGO. An explanation may be found in the chemical transformations occurring during the hydrothermal treatment of the catalysts. In the case of rGO/TiO_2-P25

synthesis, the surface hydroxyl groups of TiO_2 react with the active oxygen species of rGO surface which are then reduced during hydrothermal treatment. At the same time, and as consequence of the generated Ti-O-C bond, the surface oxygen atoms of the TiO_2 nanoparticles can diffuse to the rGO surface to balance its deoxygenation generating oxygen vacancies in TiO_2. The oxygen-enriched medium due to the high concentration of alkoxide groups during hydrothermal treatment of rGO/TiO_2-HM materials could prevent this migration, hence the generation of oxygen vacancies in rGO/TiO_2-P25 nanoparticles. It is often reported that oxygen vacancies can influence in the photocatalytic properties of TiO_2-based catalysts [40-42]. Our findings are in agreement with literature; however, effects of crystalline phase, particle size and morphology cannot be discarded at this moment, since the intensity of the EPR signal is very low as clearly observed in Figure 10.

The linear plot of $Ln(C/C_o)$ versus the treatment time for the organic constituents of SPW in presence of rGO(10%)/TiO_2-P25 (Figure 14) shows that the photocatalytic reaction rates increase as follows: acetic acid < phenols < naphthalene < xylenes < toluene. In other words, under the same experimental conditions, the hydrophobic substances are more reactive than those with hydrophilic nature, due to their higher affinity for the hydrophobic surface of the rGO nanolayers.

As it can be observed, acetic acid is barely removed. However, taking into account the biodegradable character of this compound, a possible combination of a photocatalytic process with a biological treatment could offer a costly-effective approach. On the contrary, aromatic compounds, which are known to present a low biodegradability and a higher toxicity, can be removed prior to the subsequent biological process.

These results indicated that nanocomposites of titania coupled with reduced graphene oxide can favor the photo-oxidation of organics, especially those with larger hydrophobic nature, in presence of highly saline waters. However, the nature of pristine titania (i.e. morphology, crystalline phases, particle and pore sizes) affects the photocatalytic activity of the rGO/TiO_2 nanocomposite.

4.2. Influence of rGO/TiO_2 weight ratio

The TOC removal degree is also influenced by the rGO/TiO_2 weight ratio (Fig. 15). Under the same experimental conditions, but at dark, the TOC removal degree is less than 6% for all rGO/TiO_2 weight ratios (data not shown).

Among rGO/TiO_2-P25 photocatalysts with different weight ratios (1%, 5%, 10% and 20%), the highest photocatalytic efficiency ($5.093 \cdot 10^3$ ppmTOC/kWh) is achieved over the nanocomposite prepared by employing amounts of P25 and rGO with a ratio of 10:1. This result is in accordance with the TEM (Figures 2a-d) and HRTEM analyses (Figures 5a-d) revealing that an effective photogenerated charge transfer may be related to an optimal interaction between TiO_2-P25 nanoparticles and rGO nanosheets in rGO(10%)/TiO_2 sample (Figure 2c).

The same trend is observed when the rGO/TiO_2-HM series of nanocomposites are used as photocatalysts, reinforcing the idea of that an optimum rGO/TiO_2 ratio should be given for maximum performance. Such a ratio allows better TiO_2 dispersion and components interaction within a series of hybrid photocatalysts.

4.3. Influence of hydrogen peroxide

Since hydrogen peroxide can enhance photocatalytic oxidation processes by promoting the generation of hydroxyl radicals via reaction of H_2O_2 with photogenerated electrons [44], some investigations carried out by using rGO(10%)/TiO_2-P25 nanocomposite at varying COD/H_2O_2 weight ratio are reported in Figure 16. The rate of TOC removal decreases when hydrogen peroxide is added to the reacting system, whereas the variation of COD/H_2O_2 ratio from 1:1 to 1:8 does not significantly affect the photocatalytic rate of TOC removal: an efficiency of $5.093 \cdot 10^3$ ppmTOC/kWh is recorded after 5 hours of treatment. The decrease in activity of rGO/TiO_2 composites by using selected concentrations of hydrogen peroxide is also reported by others [45] and it is ascribed to the hydroxyl radical scavenging activity of H_2O_2. Moreover, Leonardi et al. [46] hypothesize that hydrogen peroxide partially modifies the chemical nature of the rGO surface

by acting as oxidizing agent towards some superficial carbon atoms and leading to the generation of different oxygen-functional groups, such as epoxy, carbonyl, and carboxylic groups.

5. Conclusions

Saline produced water is difficult to treat through photocatalytic technologies due to the very high concentration of chloride ions. Titania coupled with reduced graphene oxide shows higher activity than bare TiO_2 nanoparticles for reducing the TOC of SPW, due to the larger BET surface areas, active phase dispersion and the reduced charge carriers recombination. In particular, rGO/TiO_2 nanocomposites, due to the hydrophobic nature of the carbonaceous phase, are more efficient at removing high hydrophobic organics, i.e. aromatics, which are generally refractory to conventional biological treatments. On the other hand, under the same experimental conditions, acetic acid is scarcely degraded and it could be successively removed through biological processes.

The present study highlights the role of physico-chemical properties in defining the catalytic efficiency of these hybrid nanocomposites in the treatment of biorefractory organic pollutants. The tested materials differ in terms of crystallographic phase composition, particle size, and morphology. In particular, XRD analyses indicate (*i*) the presence of sole anatase and anatase/rutile mixture for rGO/TiO_2-HM and rGO/TiO_2-P25 composites, respectively; (*ii*) an average crystallite size for titania nanoparticles in rGO/TiO_2-HM and rGO/TiO_2-P25 samples composites of about 6 nm and 20 nm (also confirmed by HRTEM), respectively. BET analyses indicate that: (*i*) the surface areas of TiO_2-P25 and rGO/TiO_2-P25 samples are significantly smaller than TiO_2-HM and rGO/TiO_2-HM in the whole range of rGO contents; (*ii*) the addition of reduced graphene oxide in rGO/TiO_2-P25 samples determines an increase in micropore and mesopore sizes respect to pristine TiO_2-P25 whereas it does not lead to an appreciable increase in volume of pores for rGO/TiO_2-HM composites. TEM and HRTEM analyses evidence different morphologies of the composite particles. Lamellar structures of reduced graphene oxide are observed for rGO/TiO_2-P25 samples with titania particles well dispersed on rGO nanosheets particularly in the sample with a rGO/TiO_2

weight ratio of 10%. On the contrary, rGO/TiO_2-HM samples are constituted by titania nanorods and round-shaped nanoparticles. The different rGO/TiO_2 weight ratio markedly affects the photocatalytic activity of the hybrid nanocomposites.

The higher photoactivity of pristine TiO_2-HM compared to commercial bare P25 can be related to the specific surface area of TiO_2-HM, which is three times higher than TiO_2-P25.

On the other hand, the differences in shape, phase and particle size have demonstrated to play a role in the photoactivity of these materials. Moreover, the possible presence of oxygen vacancies in the rGO/TiO_2-P25 detected by EPR analysis can also contribute to an enhancement in the photocatalytic activity, promoting electron transfer and inhibiting the electron–hole recombination process in the photocatalyst. Finally, the experimental results also indicate that the use of hydrogen peroxide should be avoided. These materials may be proposed as promising photocatalytic nanomaterials for the treatment of saline produced water, approach that has been scarcely explored, thus opening a path for an integrated cost-effective treatment for these highly recalcitrant wastewaters.

Acknowledgment

The Authors are grateful to ERASMUS-Mobility Student Program. Authors also acknowledge ACCIONA AGUA for the characterization of the sea-water used in the experiments. JL is a Serra Hunter Fellow and is grateful to ICREA Academia program and MINECO/FEDER grant ENE2015-63969.

References

[1] D. Spasiano, R. Marotta, S. Malato, P. Fernandez-Ibanez, I. Di Somma. Appl. Catal., B 170 (2015) 90–123.

[2] J. Schneider, M. Matsuoka, M. Takeuchi, J. Zhang, Y. Horiuchi, M. Anpo, D.W. Bahnemann. Chem. Rev. 114(19) (2014) 9919–9986.

[3] H. Dong, G. Zeng, L. Tang, C. Fan, C. Zhang, X. He, Y. He. Wat. Res. 79 (2015) 128–146.

[4] A. Di Paola, E. García-López, G. Marcìa, L. Palmisano. J. Hazard. Mater. 211–212 (2012) 3–29.

[5] R. Daghrir, P. Drogui, D. Robert. Ind. Eng. Chem. Res. 52(10) (2013) 3581–3599.

[6] L.W. Zhang, H.B. Fu, Y.F. Zhu. Adv. Funct. Mater. 18 (2008) 2180–2189.

[7] D.Y. Rahman, M. Rokhmat, E. Yuliza, E. Sustini, M. Abdullah. Int. J. Energy Environ. Eng. 7(3) (2016) 289–296.

[8] B.A. Bhanvase, T.P. Shende, S.H. Sonawane. Environ. Technol. Rev. 6(1) (2017) 1–14.

[9] L.Y. Ozer, C. Garlisi, H. Oladipo, M. Pagliaro, S.A. Sharief, A. Yusuf, S. Almheiri, G. Palmisano. J. Photochem. Photobiol., C Photochem. Rev. https://doi.org/10.1016/j.jphotochemrev.2017.06.003. *In press*.

[10] H. Zhang, X. Lv, Y. Li, Y. Wang, J. Li. ACS Nano 4 (2009) 380–386.

[11] Y. Gu, M. Xing, J. Zhang. Appl. Surf. Sci. 319 (2014) 8–15.

[12] Q.J. Xiang, J.G. Yu, M. Jaroniec. Chem. Soc. Rev. 41 (2012) 782–796.

[13] N. Zhang, M.Q. Yang, S. Liu, Y Sun, Y.J. Xu. Chem. Rev. 115 (2015) 10307–10377.

[14] C. Han, N. Zhang, Y.J. Xu. Nano Today 11 (2016) 351–372.

[15] K. Lee, J. Neff. Produced water environmental risks and advances in mitigation technologies, Springer 2011.

[16] M.T. Stephenson. J. Petrol. Technol. 44(5) (1992) 548–550.

[17] J. Veil, M.G. Puder, D. Elcock, R.J.J. Redweik. A White paper describing produced water from production of crude oil, natural gas and coal bed methane, Prepared for: U.S. Department of Energy National Energy Technology Laboratory Under Contract W-31-109-Eng-38 (2004).

[18] F.R. Ahmaduna, A. Pendashteh, L. Chuah Abdullah, D.R. Awang Biak, S. Siavash Madaeni, Z. Abidin. J. Hazard. Mater. 170 (2009) 530–551.

[19] A. Fakhru'l-Razi, A. Pendashteh, L.C. Abdullah, D.R. Biak, S.S. Madaeni, Z.Z. Abidin, J. Hazard. Mater. 170 (2009) 530–551.

[20] G. Li, T. An, X. Nie, G. Sheng, X. Zeng, J. Fu, Z. Lin, E.Y. Zeng. Environ. Toxicol. Chem. 26 (2007) 416–423.

[21] F.V. Santos, E.B. Azevedo, G.L. Sant'Anna Jr., M. Dezotti. Braz. J. Chem. Eng. 23(4) (2006) 451–460.

[22] P.I. Gouma, J. Lee. Transl. Mater. Res. 1 (2014) 025002.

[23] M. Sokmen, A. Ozkan. J. Photochem. Photobiol, A: Chem. 147 (2002) 77–81.

[24] W.S. Hummers, R.E. Offeman. JACS 80(6) (1958) 1339.

[25] M.G. Álvarez, D. Tichit, F. Medina, J. Llorca. Appl. Surf. Sci. 396 (2017) 821–831.

[26] B. Jiang, Y. Hengbo, T. Jiang, Y. Jiang, H. Feng, K. Chen, W. Zhou, Y. Wada. Mater. Chem. Phys. 98 (2006) 231–235.

[27] G. Vitiello, A. Pezzella, A. Zanfardino, M. Varcamonti, B. Silvestri, A. Costantini, F. Branda, G. Luciani. J. Mater. Chem. B 3 (2015) 2808-2815.

[28] G. Oskam, A. Nellore, R.L. Penn, P.C. Searson. J. Phys. Chem. B 107 (2003) 1734–1738.

[29] T.I.R. Utvik, J.R. Hasle. J. Pet. Technol. 54 (2015) 67–69.

[30] C.G. Hatchard, C.A. Parker. Proc. R. Soc. London, Ser. A 235 (1956) 518–536.

[31] S. Goldstein, J. Rabani, J. Photochem.Photobiol. A 193 (2008) 50–55.

[32] Y. Zuo. Geochim. Cosmochim. Acta 59 (1995) 3123–3130.

[33] N. López, P. Marco, J. Giménez, S. Esplugas. Appl. Catal. B 220 (2018) 497–505.

[34] Y. Liu. RSC Adv. 4 (2014) 36040–36045.

[35] S. Park, K.S. Lee, G. Bozoklu, W. Cai, S.T. Nguyen, R.S. Ruoff. ACS Nano 2 (2008) 572–578.

[36] E. Vasilaki, I. Georgaki, D. Vernardou, M. Vamvakaki, N. Katsarakis. Appl. Surf. Sci., 353 (2015) 865–872.

[37] J. Du, X.Y. Lai, N. L. Yang, J. Zhai, D. Kisailus, F.B. Su, D. Wang, L. Jiang, ACS Nano 5 (2011) 590–596.

[38] E.A. Konstantinova, A.I. Kokorin, S. Sakthivel, H. Kisch, K. Lips. Chim. Int. J. Chem. 61 (2007) 810–814.

[39] M. Alfè, D. Spasiano, V. Gargiulo, G. Vitiello, R. Di Capua, R. Marotta. Appl. Catal. A: General 487 (2014) 91–99.

[40] M. Long, Y. Qin, C. Chen, X. Guo, B. Tan, J. Phys. Chem. C 117 (2013) 16734–16741.

[41] X. Pan, N. Zhang, X. Fu, Y.J. Xu, Appl. Catal. A 453 (2013) 181-187.

[42] X. Pan, M.Q. Yang, Z. Fu, N. Zhang, Y. J. Xu, Nanoscale 5 (2013) 3601-3614.

[43] C.V. Pham, M. Krueger, M. Eck, S.Weber, E. Erdem. Appl. Phys. Lett. 104 (2014) 132102.

[44] S. K. Sharma, R. Sanghi. Advances in Water Treatment and Pollution Prevention. Springer Science & Business Media (2012).

[45] A. Sharma, B.K. Lee. J. Environ. Manage. 165 (2016) 1–10.

[46] S.G. Leonardi, D. Aloisio, N. Donato, P.A. Russo, M.C. Ferro, N. Pinna, G. Neri. ChemElectroChem 1 (2014) 617–624.

[47] H. Atout, M.G. Álvarez, D. Chebli, A. Bouguettoucha, D. Tichit, J. Llorca, F. Medina. Mater. Res. Bull. 95 (2017) 578–587.

[48] T.I.R. Utvik. Chemosphere 39(15) (1999) 2593–2606.

[49] P.J.C. Tibbetts, I.T. Buchanan, L.J. Gawel, R. Large. A Comprehensive Determination of Produced Water Composition. In Produced Water. Springer US (1992).

[50] Database, U. P. W. (2002). USGS Produced Waters Database. U.S. Department of the Interior.

[51] J.M. Neff. Bioaccumulation in Marine Organisms: Effect of Contaminants from Oil Well Produced Water. Elsevier Science Publisher (2002).

rGO/TiO_2-P25			rGO/TiO_2-HM		
Photocatalyst	*SSA* (m^2/g)	*TPV* (cm^3/g)	Photocatalyst	*SSA* (m^2/g)	*TPV* (cm^3/g)
P25	50.4	0.307	HM	152.0	0.294
rGO(1%)/P25	53.5	0.345	rGO(1%)/HM	175.9	0.267
rGO(5%)/P25	71.4	0.405	rGO(5%)/HM	179.9	0.268
rGO(10%)/P25	78.4	0.405	rGO(10%)/HM	177.1	0.293
rGO(20%)/P25	94.4	0.407	rGO(20%)/HM	169.1	0.269

Table 1

Species	Concentration (mg/L)
Chloride	$2.18 \cdot 10^4$
Carbonate	18.80
Bicarbonate	129
Bromide	74
Sulfate	$3.31 \cdot 10^3$
Sodium	$1.21 \cdot 10^4$
Magnesium	$1.38 \cdot 10^3$
Calcium	449
Potassium	425
pH	7.60
TOC	< 0.50

Table S1

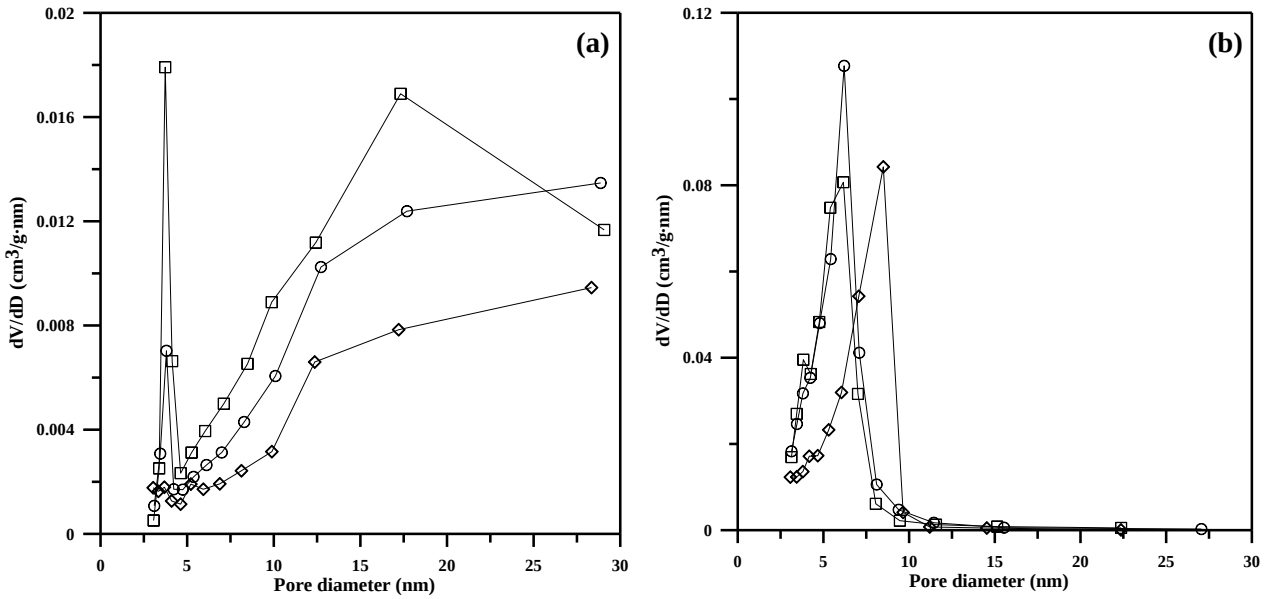
(a)
(b)
dV/dD (cm3/g·nm)
Pore diameter (nm)
0.02
0.016
0.012
0.008
0.004
0
0.12
0.08
0.04
0
5
10
15
20
25
30

Figure 1

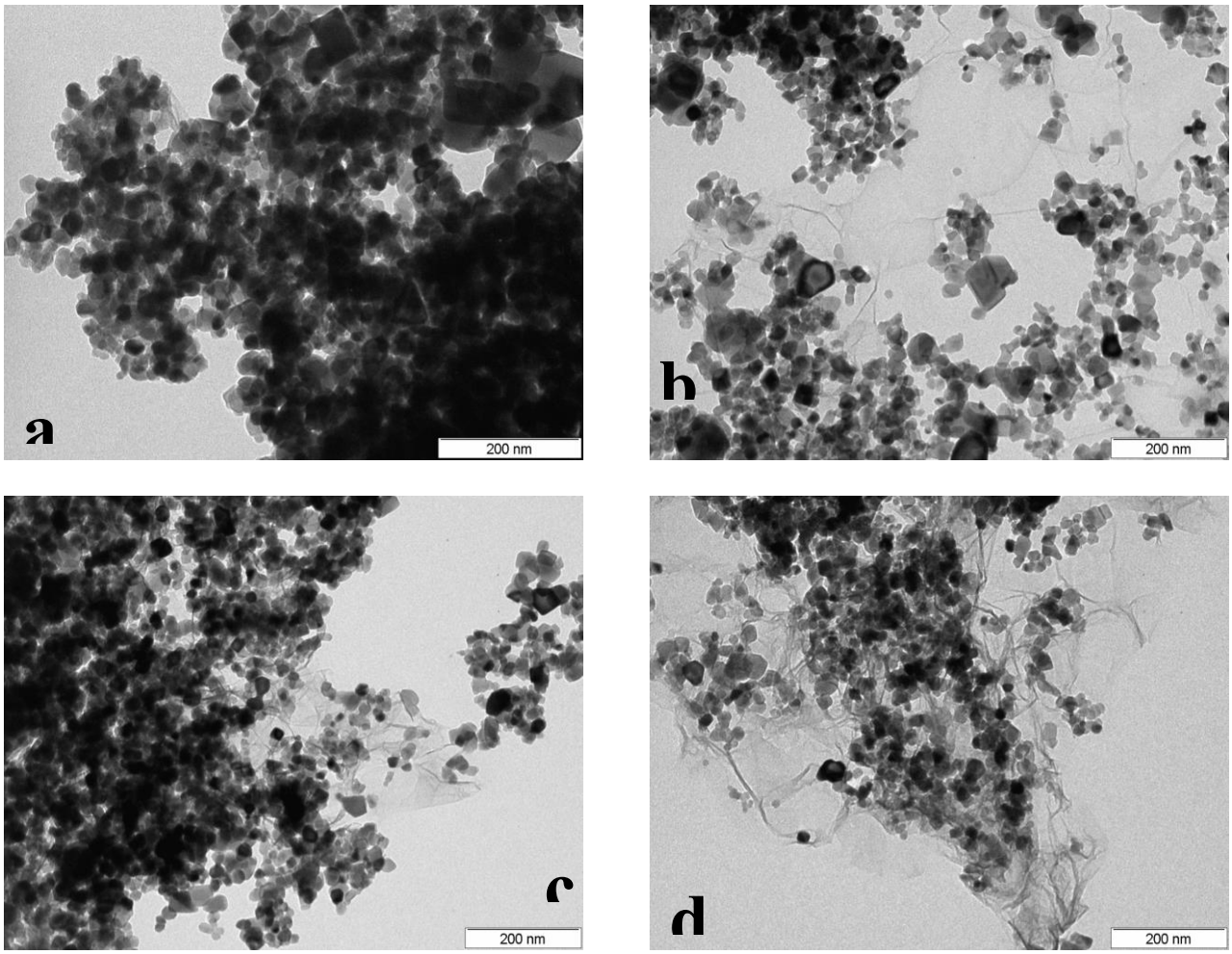

Figure 2

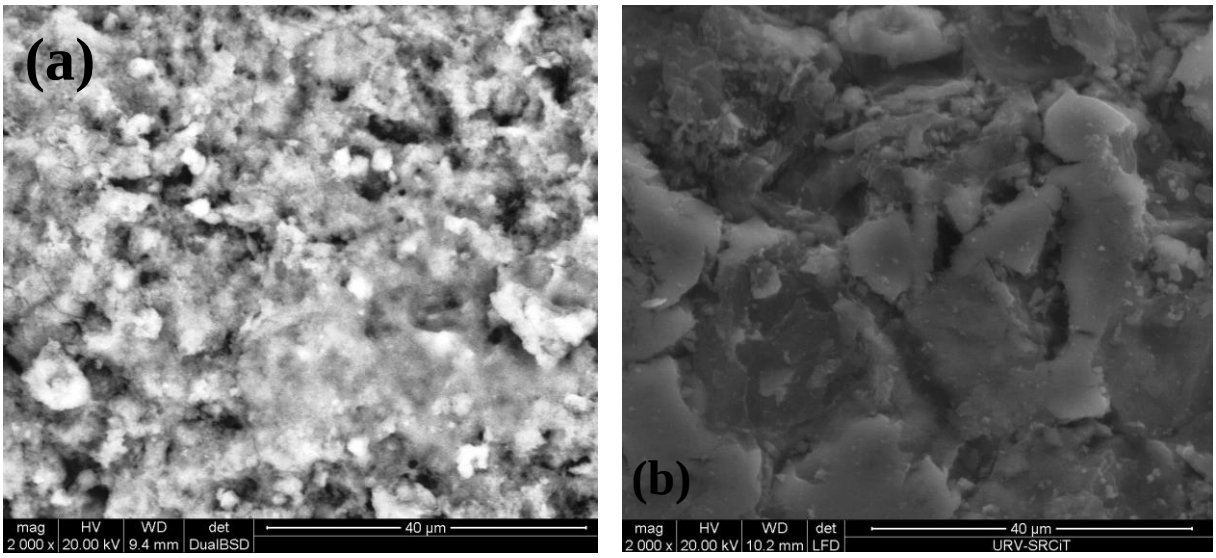
(a)
mag
2 000 x
HV
20.00 kV
WD
9.4 mm
det
DualBSD
40 µm
(b)
mag
2 000 x
HV
20.00 kV
WD
10.2 mm
det
LFD
40 µm
URV-SRCiT

Figure 3

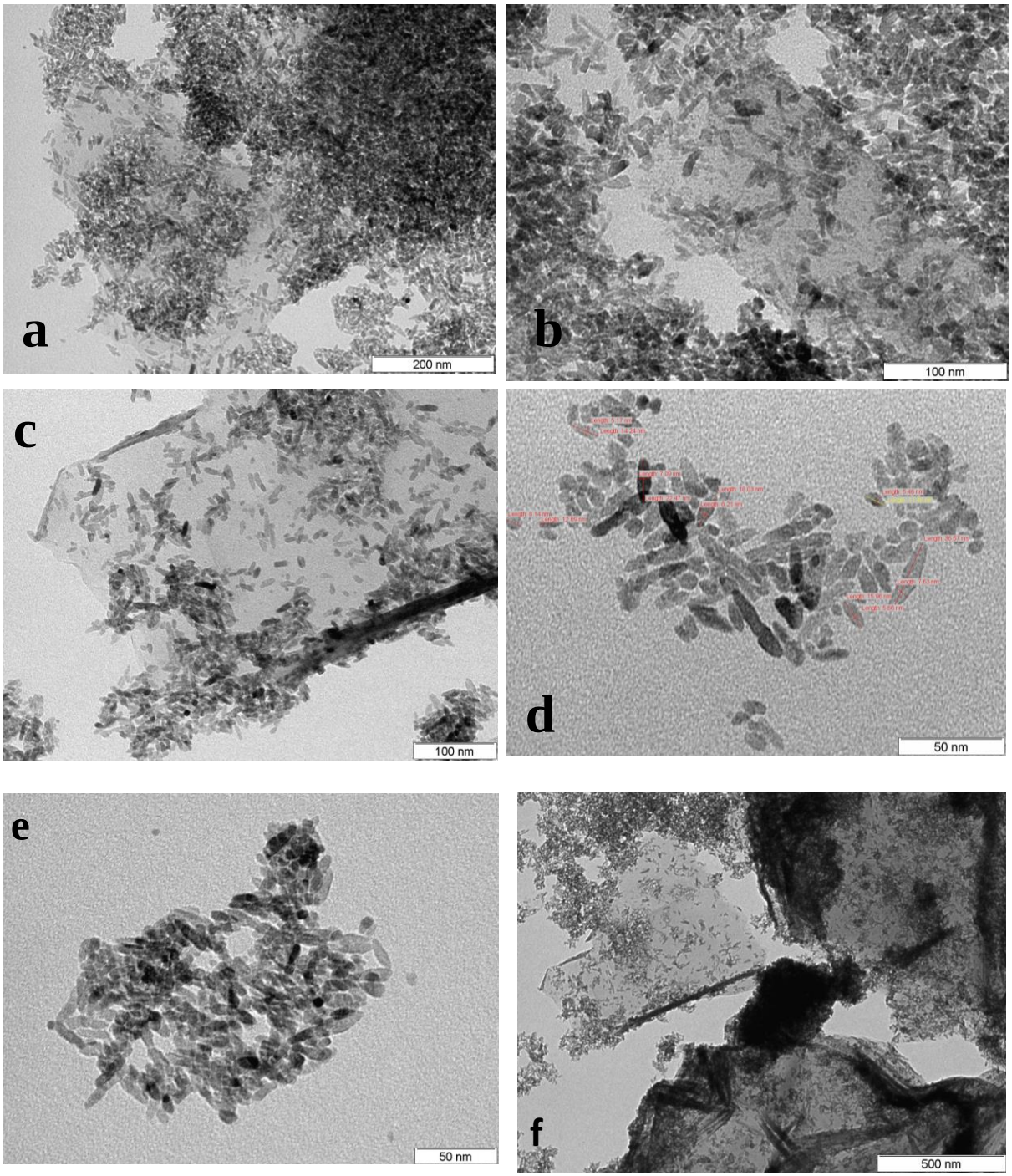

Figure 4

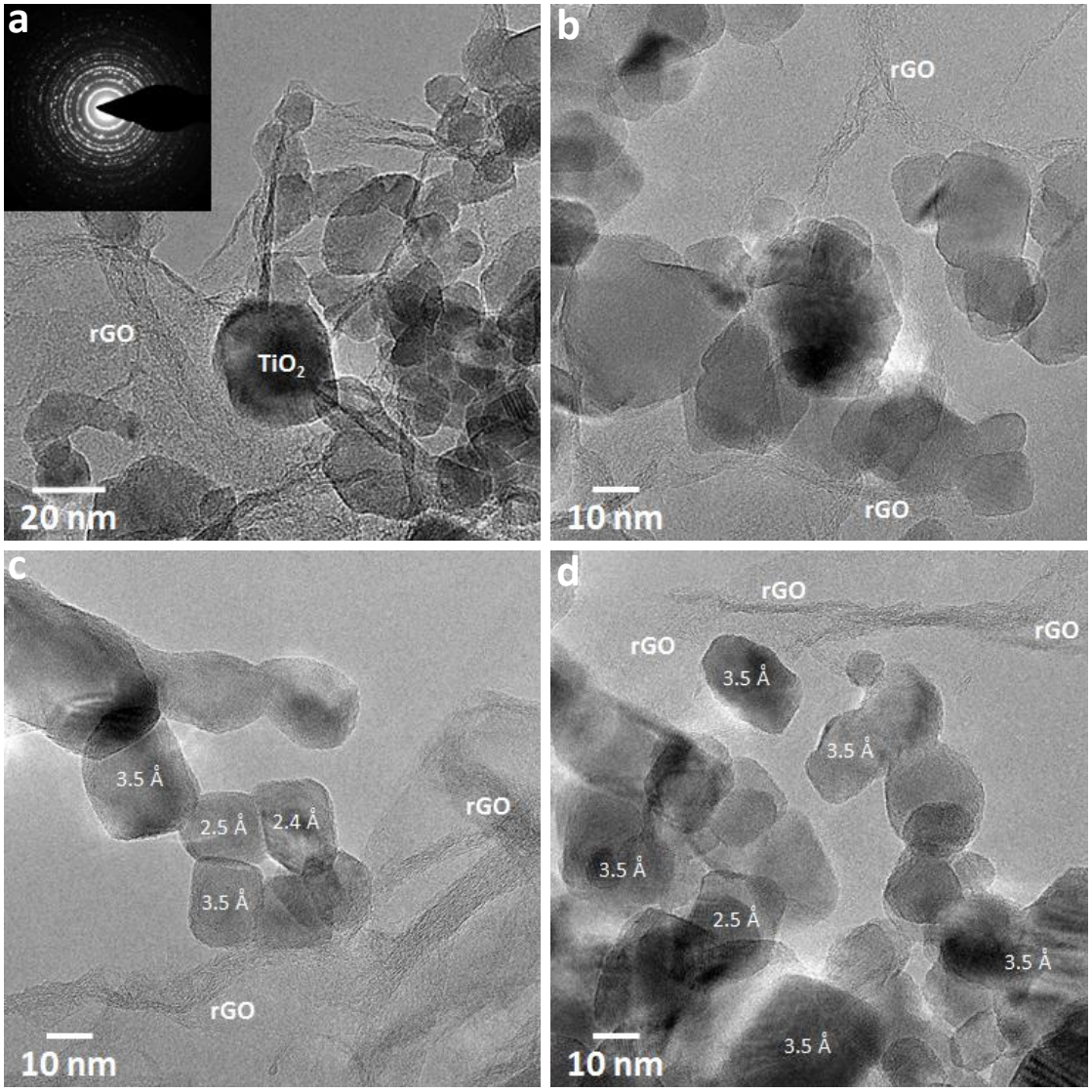
a
rGO
TiO_2
20 nm
b
rGO
10 nm
rGO
c
3.5 Å
2.5 Å
2.4 Å
rGO
3.5 Å
rGO
10 nm
d
rGO
rGO
rGO
3.5 Å
3.5 Å
3.5 Å
2.5 Å
3.5 Å
3.5 Å
10 nm

Figure 5

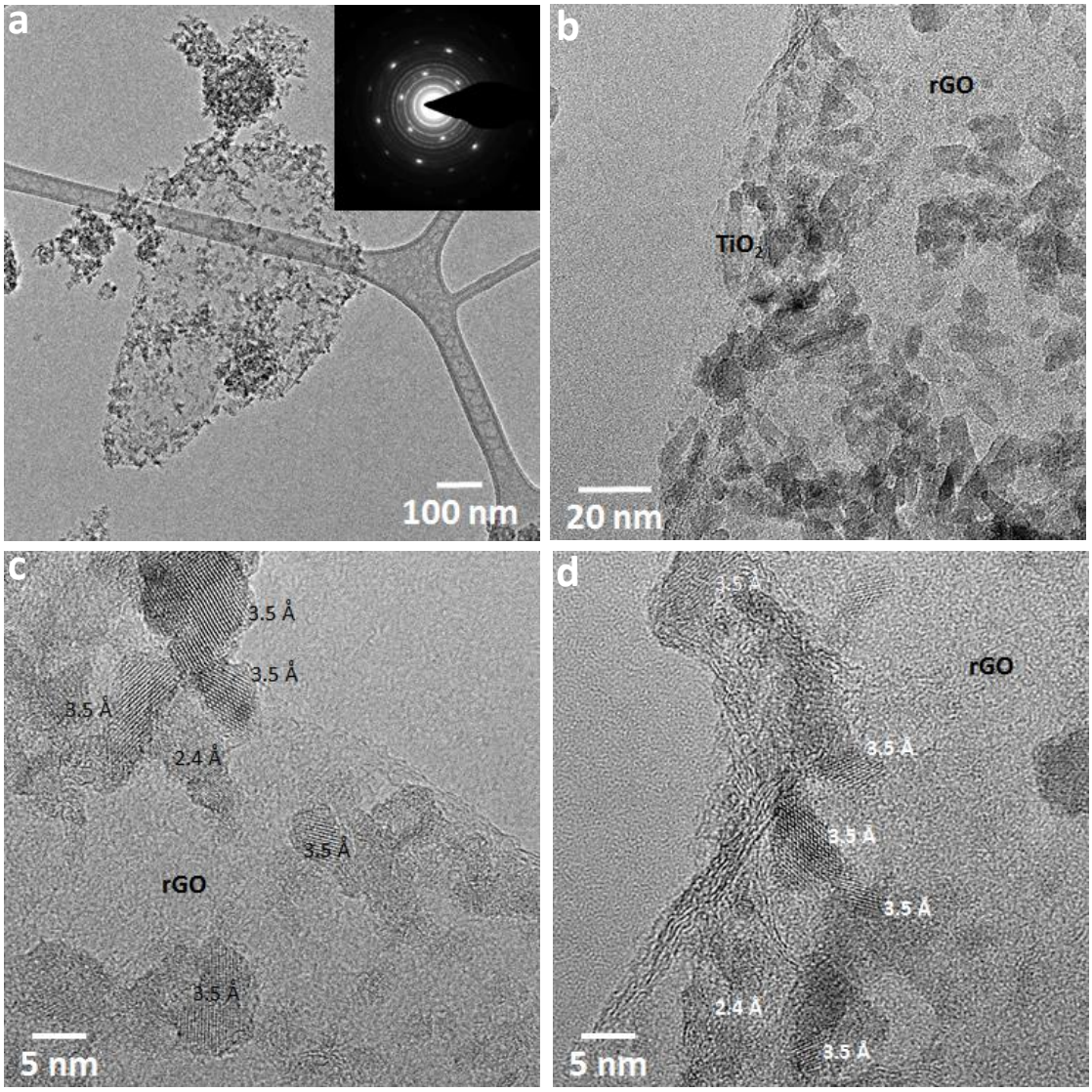
a
100 nm
b
rGO
TiO_2
20 nm
c
3.5 Å
3.5 Å
3.5 Å
2.4 Å
3.5 Å
rGO
3.5 Å
5 nm
d
3.5 Å
rGO
3.5 Å
3.5 Å
3.5 Å
2.4 Å
3.5 Å
5 nm

Figure 6

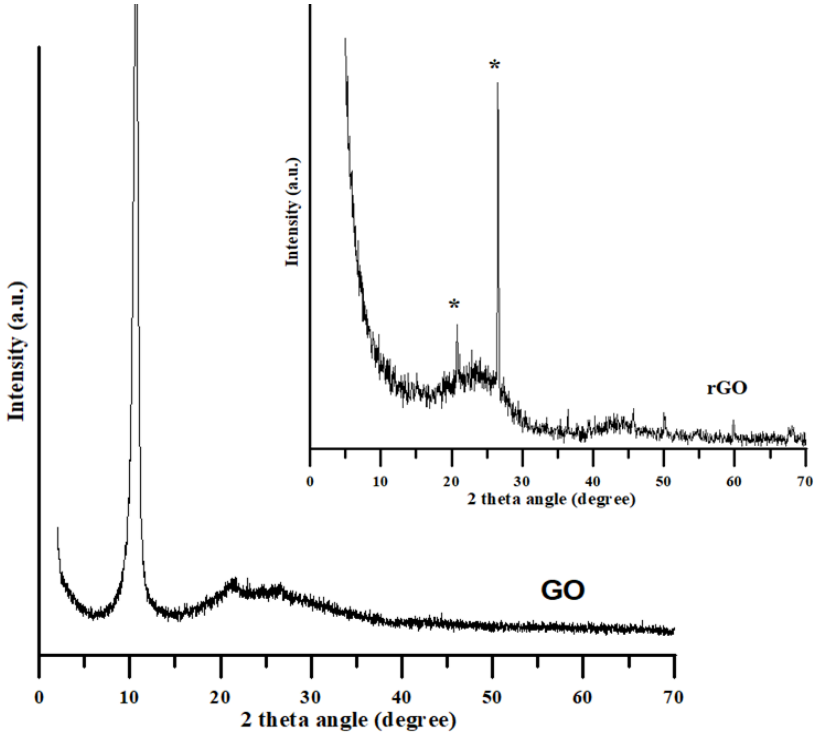
Intensity (a.u.)
GO
0
10
20
30
40
50
60
70
2 theta angle (degree)
*
*
Intensity (a.u.)
rGO
0
10
20
30
40
50
60
70
2 theta angle (degree)

Figure 7

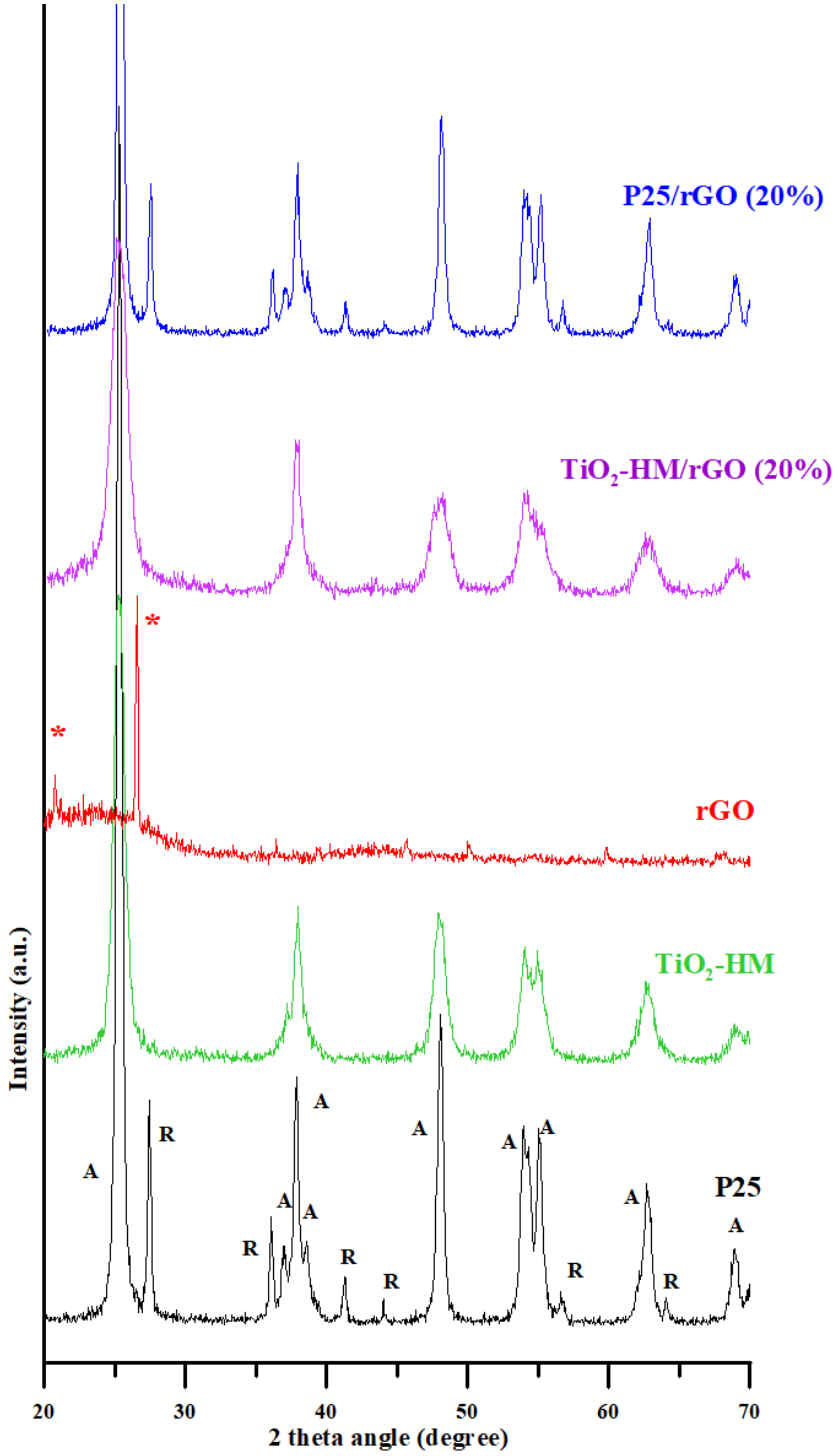
P25/rGO (20%)
TiO2-HM/rGO (20%)
rGO
TiO2-HM
P25
Intensity (a.u.)
2 theta angle (degree)
20
30
40
50
60
70
A
R
*

Figure 8

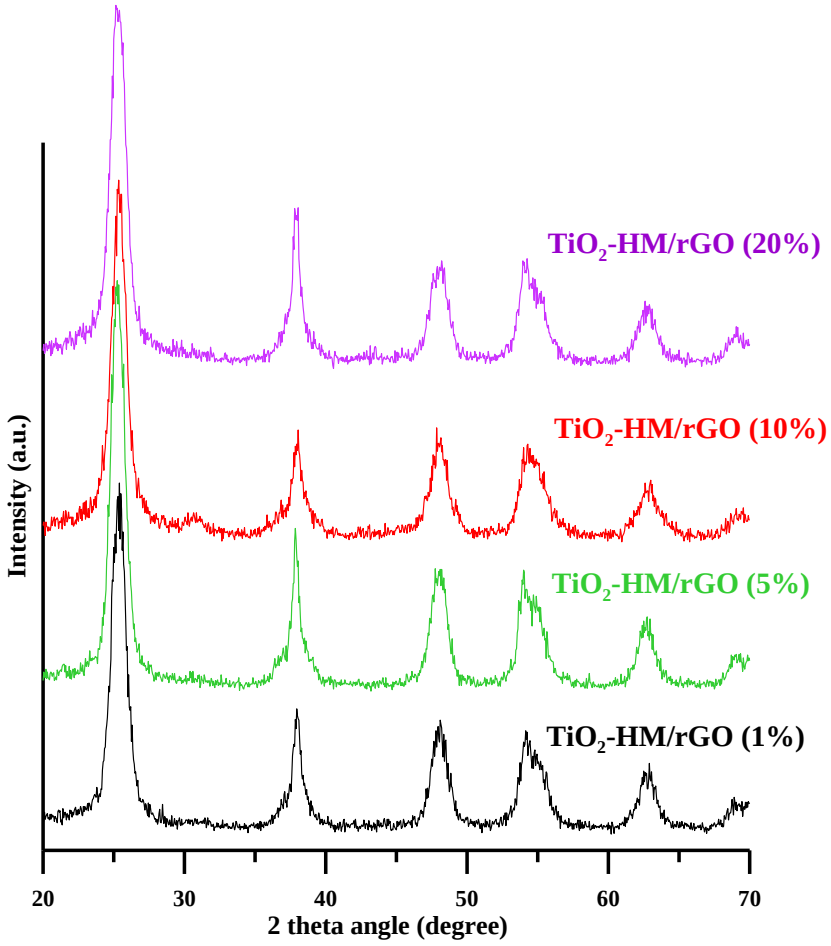
TiO2-HM/rGO (20%)
TiO2-HM/rGO (10%)
TiO2-HM/rGO (5%)
TiO2-HM/rGO (1%)
Intensity (a.u.)
20
30
40
50
60
70
2 theta angle (degree)

Figure 9

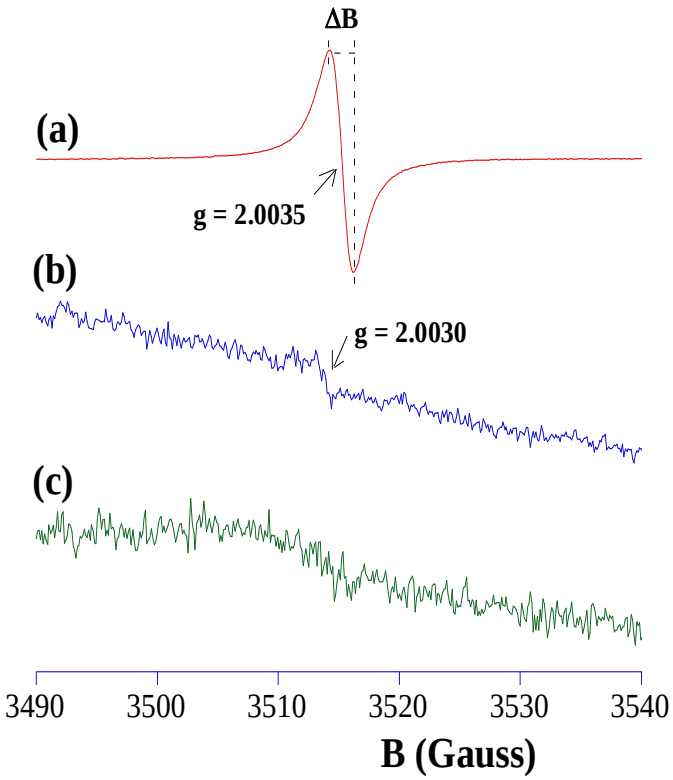

Figure 10

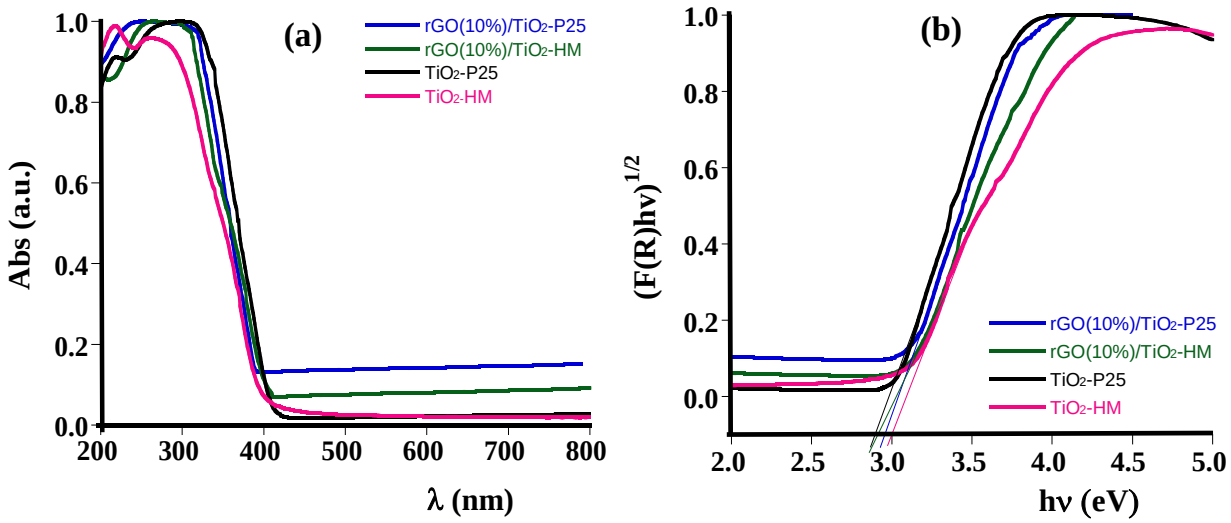
(a)
rGO(10%)/TiO2-P25
rGO(10%)/TiO2-HM
TiO2-P25
TiO2-HM
Abs (a.u.)
λ (nm)
(b)
(F(R)hν)1/2
hν (eV)

Figure 11

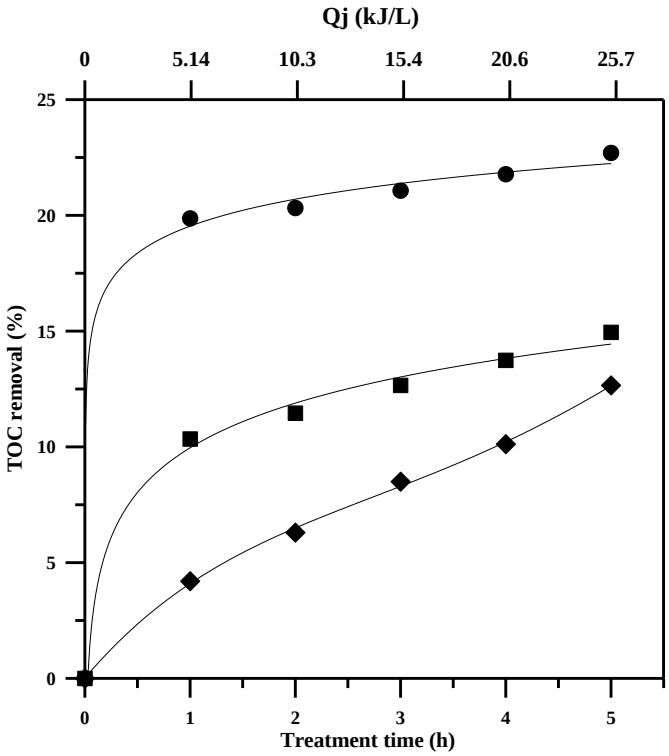
Qj (kJ/L)
0
5.14
10.3
15.4
20.6
25.7
25
20
15
10
5
0
TOC removal (%)
0
1
2
3
4
5
Treatment time (h)

Figure 12

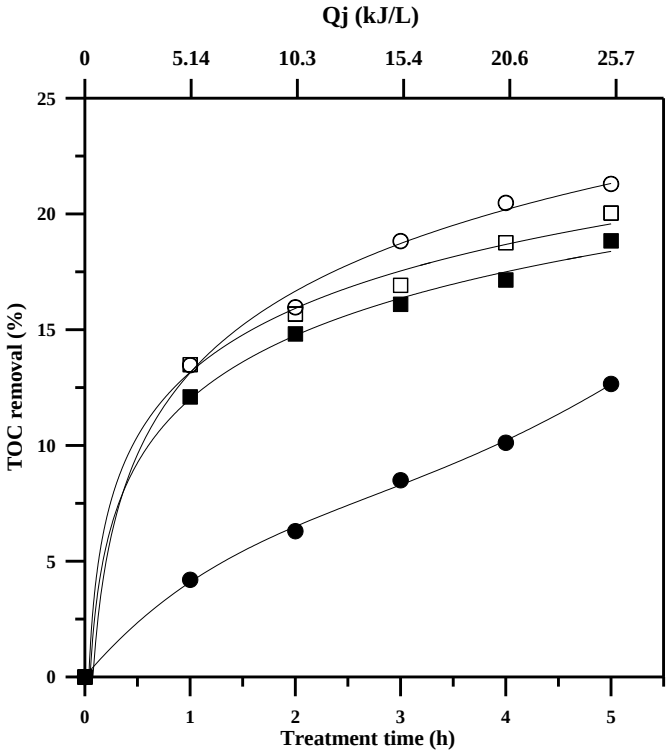
Qj (kJ/L)
0
5.14
10.3
15.4
20.6
25.7
25
20
15
10
5
0
TOC removal (%)
0
1
2
3
4
5
Treatment time (h)

Figure 13

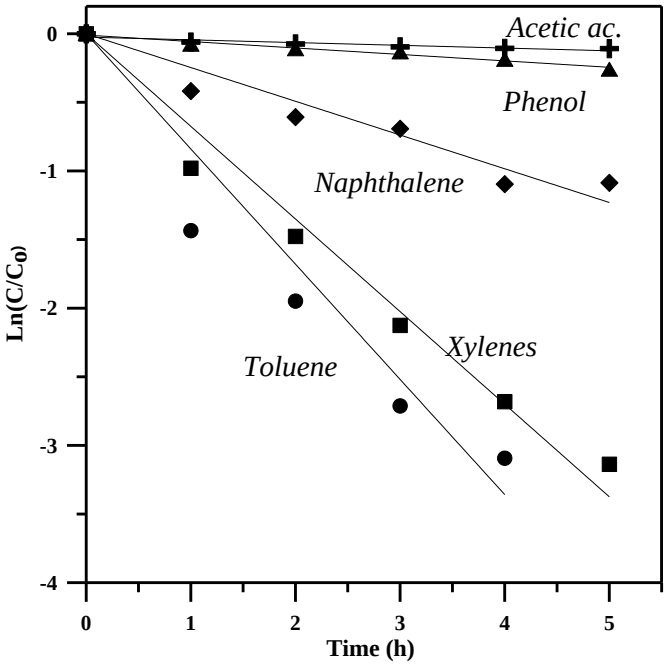
Acetic ac.
Phenol
Naphthalene
Xylenes
Toluene
Ln(C/C0)
Time (h)
0
-1
-2
-3
-4
0
1
2
3
4
5

Figure 14

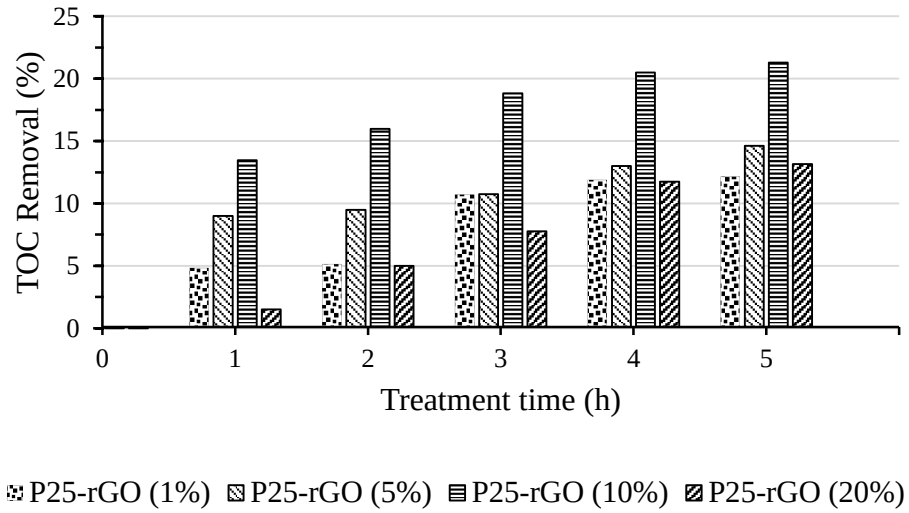
25
20
15
10
5
0
TOC Removal (%)
0
1
2
3
4
5
Treatment time (h)
P25-rGO (1%)
P25-rGO (5%)
P25-rGO (10%)
P25-rGO (20%)

Figure 15

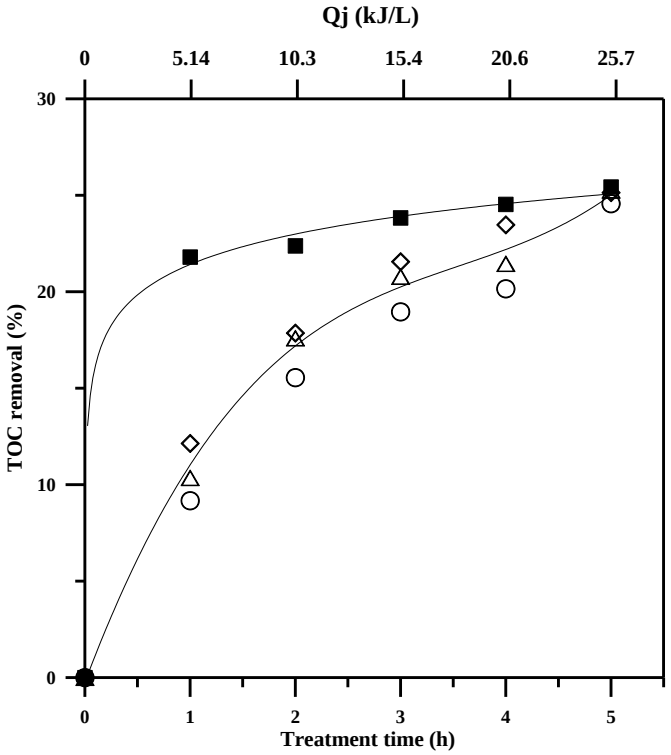
Qj (kJ/L)
0
5.14
10.3
15.4
20.6
25.7
30
20
10
0
TOC removal (%)
0
1
2
3
4
5
Treatment time (h)

Figure 16